



Contents lists available at ScienceDirect

Medical Image Analysis

journal homepage: www.elsevier.com/locate/media

A homotopy-based sparse representation for fast and accurate shape prior modeling in liver surgical planning

Guotai Wang^a, Shaoting Zhang^b, Hongzhi Xie^c, Dimitris N. Metaxas^d, Lixu Gu^{a,*}^a School of Biomedical Engineering, Shanghai Jiao Tong University, Shanghai, China^b Department of Computer Science, University of North Carolina at Charlotte, NC, USA^c Peking Union Medical College Hospital, Beijing, China^d Department of Computer Science, Rutgers University, Piscataway, NJ, USA

ARTICLE INFO

Article history:

Received 20 April 2014

Received in revised form 28 August 2014

Accepted 10 October 2014

Available online 23 October 2014

Keywords:

Sparse shape composition

Shape prior

Segmentation

Fast optimization

Scalability

ABSTRACT

Shape prior plays an important role in accurate and robust liver segmentation. However, liver shapes have complex variations and accurate modeling of liver shapes is challenging. Using large-scale training data can improve the accuracy but it limits the computational efficiency. In order to obtain accurate liver shape priors without sacrificing the efficiency when dealing with large-scale training data, we investigate effective and scalable shape prior modeling method that is more applicable in clinical liver surgical planning system.

We employed the Sparse Shape Composition (SSC) to represent liver shapes by an optimized sparse combination of shapes in the repository, without any assumptions on parametric distributions of liver shapes. To leverage large-scale training data and improve the computational efficiency of SSC, we also introduced a homotopy-based method to quickly solve the L_1 -norm optimization problem in SSC. This method takes advantage of the sparsity of shape modeling, and solves the original optimization problem in SSC by continuously transforming it into a series of simplified problems whose solution is fast to compute. When new training shapes arrive gradually, the homotopy strategy updates the optimal solution on the fly and avoids re-computing it from scratch.

Experiments showed that SSC had a high accuracy and efficiency in dealing with complex liver shape variations, excluding gross errors and preserving local details on the input liver shape. The homotopy-based SSC had a high computational efficiency, and its runtime increased very slowly when repository's capacity and vertex number rose to a large degree. When repository's capacity was 10,000, with 2000 vertices on each shape, homotopy method cost merely about 11.29s to solve the optimization problem in SSC, nearly 2000 times faster than interior point method. The dice similarity coefficient (DSC), average symmetric surface distance (ASD), and maximum symmetric surface distance measurement was $94.31 \pm 3.04\%$, 1.12 ± 0.69 mm and 3.65 ± 1.40 mm respectively.

© 2014 Elsevier B.V. All rights reserved.

1. Introduction

Primary liver cancer is one of the most life-threatening cancers around the world. In China, liver cancer is the second leading source of cancerous death, with a mortality rate of 26.26 per 100,000 people (Chen and Zhang, 2011). Among the variety of treatment methods, liver transplantation and liver resection are the most effective ones (Sotiropoulos et al., 2009). Considering the lack of available liver from cadaver, living donor liver transplantation (LDLT) is very important to extend the scarce donor pool (Broelsch et al., 2000).

A detailed knowledge of liver anatomy plays a key role in the determination of surgery strategy for LDLT. The volume of transplanted liver portion should be sufficient for the recipient and the remaining portion should be as large as possible to minimize trauma to the donor. Besides, since anatomies of intrahepatic vessels and tumors vary enormously among different patients, surgeons need to learn the location of the liver portion that would be cut off, together with the distribution of intrahepatic vessels and tumors before the surgery to achieve the best proposal for resection. As a result, preoperative planning based on medical image is highly helpful for the accuracy and safety of liver surgery.

Segmentation of liver from preoperative images is a key module in liver surgical planning. However, two important factors put forward a big challenge for accurate and robust segmentation of

* Corresponding author.

E-mail address: lixugu@sjtu.edu.cn (L. Gu).

liver in clinical environment (Heimann et al., 2009). First, the low contrast and weak boundary information in medical images can easily lead to mis-segmentation. For example, gray levels of the liver and its adjacent tissues are very similar, which renders the boundary hard to detect. Second, intrahepatic tumors often cause inhomogeneous gray levels and misleading boundaries, so these tissues may not be successfully preserved in segmentation results. These factors make prior information about liver shapes highly significant for accurate segmentation.

Shape prior-based approaches are more stable against local image artifacts than traditional methods that solely rely on low-level appearance cues. For instance, shape prior has been widely incorporated into watershed (Hamarneh and Li, 2009), geodesic active contours (Leventon et al., 2000), level set (Cremers et al., 2007; Rousson and Paragios, 2000), graph cuts (Vu and Manjunath, 2008), and it plays an important role in robust segmentation of a variety of organs such as left ventricle (Zhu et al., 2009), kidney (Xie et al., 2005), liver (Heimann et al., 2006), prostate (Ghose et al., 2012, 2010), and brain structures (Shen et al., 2001), etc.

In the application of liver surgical planning, there are two important requirements on shape prior modeling for liver. First, the shape prior should be patient-specific and accurate enough. This is because liver shapes from different individuals have very complex variations, and tumors often make liver shapes more complex. A patient-specific shape prior should contain enough prior information about a specific patient, otherwise the complex liver shape variations may lead to a big difference between shape priors and actual liver shapes for the patients, in which case the inaccurate shape priors will not help segmentation process so well. In addition, the shape prior modeling process should be scalable and efficient. Accurate liver shape modeling requires a large-scale training data and high number of vertices on liver shapes. To be applicable in clinical environment, the shape prior modeling method should remain a low-level of time consumption when training data and vertex number increase to a large scale. In addition, in many cases training shapes are collected gradually. When new training shapes arrive, the model should be updated on the fly with a high requirement on efficiency.

One of the most popular shape prior modeling methods is to use statistical shape models (SSM) to learn the priori information of shape variations from many training samples and employ it to represent an input shape adaptively (Heimann and Meinzer, 2009). The Active Shape Model (ASM) (Cootes et al., 1995) is widely used to deal with shapes that follow a unimodal Gaussian distribution. When shape variations are complex, a mixture of Gaussians may be able to handle them (Cootes and Taylor, 1999), assuming shapes follow a multimodal distribution. To overcome the limitation of ASM on statistical constraint, manifold learning techniques (Etyngier et al., 2007) can be employed to obtain a non-linear shape prior. Alternatively, the shape space can be divided into multiple sub-spaces in which shape distributions are more compact and easier to model. These methods include population-based and patient-specific shape statistics (Shi et al., 2008; Yan et al., 2011; Zhang et al., 2011), hierarchical ASM (Davatzikos et al., 2003), and subject-specific dynamical model (Zhu et al., 2009), etc.

In the recent years, sparse representation has proven to be extremely powerful to obtain a compact high-fidelity representation of the observed signal. It has also been increasingly used in a lot of image processing applications (Wright et al., 2010), where using sparsity as a prior led to state-of-the-art results. Gao et al. (2012) proposed a sparse representation based classification method and applied it to prostate segmentation. Shi et al. (2014) employed a patch-based sparse representation in neonatal atlas construction and successfully recovered more anatomical details. Sparse Shape Composition (SSC) (Zhang et al., 2012a) is a recently

proposed method for shape prior modeling. It does not need any assumption on shapes' parametric probability distribution but can effectively model complex shape variations. It is also able to capture gross errors in the input shapes and preserve local details even when they are not statistically significant in the repository (Zhang et al., 2012a). Due to these advantages, SSC has been successfully applied in cardiac motion analysis (Yu et al., 2013), lung localization and other applications (Zhang et al., 2012a). It also showed a great advantage in robust liver shape modeling (Wang et al., 2013). However, its computational efficiency may be limited by increasing repository's capacity and number of vertices on each shape. To obtain efficient shape modeling, one may decrease the repository's capacity or the number of vertices, but the accuracy will also be reduced. Dictionary learning method can improve the speed of computation by reducing redundancy of the shape repository (Zhang et al., 2012b). However, the dictionary still inevitably loses important shape information and it needs to be updated every time when new shapes are added to the repository.

A widely-used optimization scheme to solve SSC is the interior point method. It can achieve the optimal solution conveniently but has a high complexity, which precludes its application when the problem is on a large-scale (Beck and Teboulle, 2009). Gradient-based methods are more efficient since they usually make use of the sparsity of the problem. For example, the iterative shrinkage-thresholding algorithm (ISTA) and the fast iterative shrinkage-thresholding algorithm (FISTA) have been successfully used in signal/image processing with fast speed (Beck and Teboulle, 2009). Other fast L_1 -minimization algorithms include the augmented Lagrange multiplier (ALM) method (Afonso et al., 2011), iteratively reweighted algorithms (Chartrand and Wotao, 2008), and primal-dual algorithms (Chambolle and Pock, 2011), with their application in image restoration, reconstruction, denoising, etc. Homotopy (Foucart and Rauhut, 2013) is substantially faster than interior point method. It continuously transforms the L_1 optimization problem into a series of simplified problems whose solution is fast to compute (Malioutov et al., 2005). Homotopy is more efficient than other methods such as FISTA and ALM in sparse representation problems of face recognition (Yang et al., 2010). It has also been used as a highly effective way to solve the L_1 optimization problem in many other fields, such as the recovery of streaming signals (Asif and Romberg, 2013) and highly undersampled image reconstruction (Trzasko and Manduca, 2009).

On the other hand, in many medical imaging applications such as liver image segmentation based on statistical shape models, training shapes may not come in on batch. This is because it is hard to obtain a training shape with a large number of vertices in real-time, and constructing an informative shape repository with a large capacity is extremely time consuming. As a result, new training shapes are gradually added to an existing shape repository. In this case, the optimization of shape modeling should be updated when new training shapes come. A direct way to solve this problem is to re-compute the optimal solution using the expanded repository, disregarding the solution obtained from the previous repository. However, this method has a low efficiency. A better way is to take advantage of the previous solution and compute the new one in a faster speed.

The combination of SSC and homotopy was preliminarily investigated by Wang et al. (2014). However, the property of homotopy and SSC was not discussed in detail. In this paper, we study the applicability of homotopy-based SSC in liver shape modeling to a further degree and investigate its performance when updating the modeling on the fly. The new method can improve the accuracy of SSC-based liver shape modeling by using a large-scale training data and high number of vertices on each shape. The runtime of the new method just increases very slowly when the scale of training samples and the number of vertices grow to a large scale. In

addition, our method also aims to address the efficient optimization problem in shape modeling on the fly. When new shapes are added to the repository, homotopy-based SSC can achieve the new solution from a warm-start solution taking advantage of the previous one, which is much faster than re-computing the solution from scratch. Thus, the homotopy-based SSC can be more scalable and applicable in real-time clinical applications.

2. Methods

The workflow of liver shape prior modeling is shown in Fig. 1. It consists of offline learning, runtime shape modeling and updating on the fly. In offline learning, liver image data from a large range of individuals are collected and manually segmented, and segmentation results are converted to shape representation. After a shape alignment and correspondence process, the training shapes constitute a liver shape repository. In runtime shape modeling, an initial segmentation of an input image data is implemented. The segmentation result is represented as a polygonal shape for the input of SSC. We construct a $L1$ -regulated optimization problem of sparse representation between the input shape and liver shape repository, which is solved by homotopy method. The output of SSC is taken as the shape prior for liver related to the input image data. When new training shapes are added to the repository, the optimal solution for SSC is updated on the fly, which can obtain a new optimized shape representation in a fast speed.

2.1. Sparse shape composition

SSC represents an input shape by a sparse combination of shapes in the repository. A shape is denoted as a column vector that is formed by stacking coordinates of all the vertices. A shape containing l vertices with the dimensionality of p can be represented by a vector $\mathbf{d} \in R^m$, where $m = l \times p$. If a training repository consists of n shapes, the i th shape can be denoted as \mathbf{d}_i , and all the training shapes can be arranged as a matrix $D = [\mathbf{d}_1, \mathbf{d}_2, \dots, \mathbf{d}_n] \in R^{m \times n}$. All the training shapes are pre-aligned using generalized Procrustes analysis (Cootes et al., 1995), in order to put them in a common coordinate system. Considering an input shape $\mathbf{y} \in R^m$, it can be transformed to the common canonical space of D by a spatial transformation operator T with a parameter vector β . The transformation result is $\mathbf{y}' = T(\mathbf{y}, \beta)$. The SSC representation is obtained by solving the following $L1$ -norm optimization problem:

$$\arg \min_{\mathbf{x}, \mathbf{e}} \{ \|\mathbf{x}\|_1 + \xi \|\mathbf{e}\|_1 \}, \quad s.t. \|\mathbf{y}' - D\mathbf{x} - \mathbf{e}\|_2 \leq \eta \quad (1)$$

where $\mathbf{x} \in R^n$ denotes the coefficients for training samples, and $\mathbf{e} \in R^m$ represents the gross errors in the input shape. The minimization of $L1$ -norm $\|\mathbf{x}\|_1 + \xi \|\mathbf{e}\|_1$ generally enforces the sparsity of shapes in the repository and that of gross error. ξ controls the weight between the sparsity of \mathbf{x} and that of \mathbf{e} . We call $D\mathbf{x} + \mathbf{e}$ the

SSC represented shape. The $L2$ -norm term measures the difference between the input shape and the SSC represented shape, and it denotes the accuracy of the sparse representation result. By solving this $L1$ -norm optimization problem, the combination of shapes in the repository is obtained as $D\mathbf{x}$, and it is transformed back to the original coordinate space of \mathbf{y} , thus the output of SSC is accepted as $\mathbf{y}'' = T^{-1}(D\mathbf{x}, \beta)$.

2.2. Optimization via Linear Programming (LP)

The problem in Eq. (1) can be converted to a LP problem and solved by interior point methods, which have a complexity of polynomial time. At each iteration, the LP method will invert a $(n + m) \times (n + m)$ matrix, and the complexity will be $O((n + m)^3)$. This method may be well used when the repository's capacity and vertex number are small. However, the problem of liver shape representation is often large-scale, and the potential advantage of sophisticated interior point methods will often be precluded (Beck and Teboulle, 2009).

2.3. Optimization via proximal gradient

The problem of Eq. (1) can be converted to the following equivalent one:

$$\arg \min_{\mathbf{x}, \mathbf{e}} \left\{ \frac{1}{2} \|\mathbf{y}' - D\mathbf{x} - \mathbf{e}\|_2^2 + \lambda (\|\mathbf{x}\|_1 + \xi \|\mathbf{e}\|_1) \right\} \quad (2)$$

where λ controls the weight between the $L2$ - and $L1$ -norm. \mathbf{x} and \mathbf{e} can be stacked to form a new vector $\mathbf{x}' \in R^{n+m}$, thus the problem in Eq. (2) can be converted to an equal optimization problem that deals with just one variable \mathbf{x}' . We define $A = [D \ I(m)] \in R^{m \times (n+m)}$, where $I(m)$ is a unit matrix of size m . Thus, Eq. (2) can be written as:

$$\arg \min_{\mathbf{x}'} F_{(\lambda)}(\mathbf{x}') = \arg \min_{\mathbf{x}'} \left\{ \frac{1}{2} \|\mathbf{y}' - A\mathbf{x}'\|_2^2 + \lambda \|\mathbf{x}'\|_1 \right\} \quad (3)$$

where the $L1$ -norm is defined as $\|\mathbf{x}'\|_1 = \|\mathbf{x}\|_1 + \xi \|\mathbf{e}\|_1$.

Gradient-based methods for solving Eq. (3) are obviously more efficient than LP, since the main computational cost of these methods is due to matrix-vector multiplication related to A or A^T . One of the most popular gradient-based methods is the iterative shrinkage-thresholding algorithm (ISTA) (Daubechies et al., 2004). The computational cost of ISTA is relatively cheap. The advantage of ISTA is its simplicity. However, it has also been recognized as a slow method with a worst-case convergence of $O(1/k)$. The fast iterative shrinkage-thresholding algorithm (FISTA) was proposed to accelerate the convergence rate of ISTA (Beck and Teboulle, 2009). FISTA considers a method that is similar to ISTA, and it preserves the computational simplicity of ISTA but has a global better rate of convergence which is $O(1/k^2)$ (Nesterov, 1983).

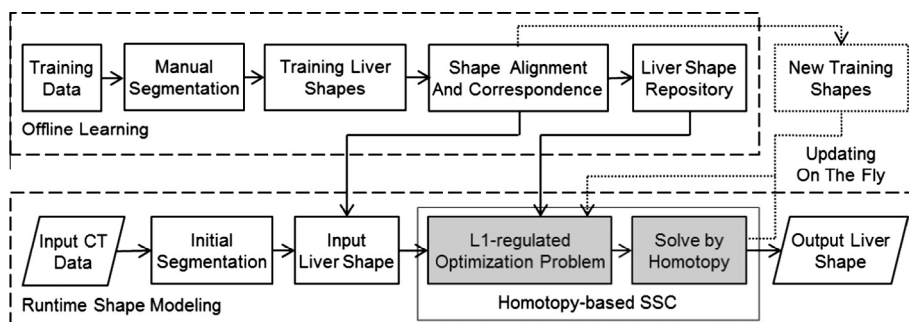


Fig. 1. Workflow of liver shape prior modeling using homotopy-based SSC. The two gray blocks show our key contributions in the whole system.

2.4. Optimization via homotopy method

Homotopy method exploits a simple geometric property of the solution space of Eq. (3), and it traces solutions of Eq. (3) from one value of λ to another lower value. At a large value of λ , the sparsity of shapes and gross errors are favored. With the decrease of λ , the accuracy of the optimal solution has a relative higher weight. We use $\mathbf{x}'_{(\lambda)}$ to represent the optimal solution at a certain value of λ . When $\lambda \rightarrow \infty$, $\mathbf{x}'_{(\lambda)}$ becomes 0; when $\lambda \rightarrow 0$, $\mathbf{x}'_{(\lambda)}$ converges to the solution of Eq. (1). We can define $\chi = \{\mathbf{x}'_{(\lambda)} : \lambda \in [0, \infty)\}$, and it identifies a solution path resulting from the change of λ from ∞ to 0.

The subdifferential of $F_{(\lambda)}(\mathbf{x}')$ in Eq. (3) is defined as:

$$\partial F_{(\lambda)}(\mathbf{x}') = A^T(A\mathbf{x}' - \mathbf{y}') + \lambda \partial \|\mathbf{x}'\|_1 \quad (4)$$

where the subdifferential of the $L1$ -norm is given by

$$\partial \|\mathbf{x}'\|_1 = \{\mathbf{v} \in R^{n+m} : \mathbf{v}_j = \partial |\mathbf{x}'_j|, j = 1, 2, \dots, n+m\} \quad (5)$$

$$\partial |\mathbf{x}'_j| = \begin{cases} \text{sgn}(\mathbf{x}'_j) & \text{if } \mathbf{x}'_j \neq 0 \\ [-1, 1] & \text{if } \mathbf{x}'_j = 0 \end{cases}, \quad j = 1, 2, \dots, n+m \quad (6)$$

To achieve the optimal solution of Eq. (3), the subdifferential of $F_{(\lambda)}(\mathbf{x}')$ should be set to zero. This is equivalent to

$$\begin{cases} (A^T(A\mathbf{x}' - \mathbf{y}'))_j = -\lambda \text{sgn}(\mathbf{x}'_j) & \text{if } \mathbf{x}'_j \neq 0 \\ |(A^T(A\mathbf{x}' - \mathbf{y}'))_j| \leq \lambda & \text{if } \mathbf{x}'_j = 0 \end{cases} \quad (7)$$

The support set of $\mathbf{x}'_{(\lambda)}$ is denoted as Γ . At any value of λ , the optimal solution $\mathbf{x}'_{(\lambda)}$ is completely determined by Γ and its sign sequence (Asif and Romberg, 2013). Γ changes only at certain nodes of λ , and the solution path χ follows a continuous, piecewise-linear function of λ (Osborne et al., 2000; Yang et al., 2010; Donoho and Tsaig, 2008). To achieve a decreasing sequence of λ , one just need to identify break-points that lead to changes of the support set Γ (Asif and Romberg, 2013). The property of homotopy is illustrated in Fig. 2 for a simple sparse shape representation problem. The input shape was constructed by a sparse combination of shapes in the repository and it contained no gross error. This simplified problem just dealt with \mathbf{x} , and it optimized the representation coefficient of each training shape. Fig. 2(b) shows the solution path with decrease of λ . The homotopy algorithm started with a large value of λ , where the solution was $\mathbf{x} = 0$. White dot lines showed break points where the support set Γ changed. When λ was decreased to a certain number, the solution reached the representation coefficients used in Fig. 2(a).

At each iteration, homotopy will find a new break point, and Γ should be updated. In the problem of liver shape modeling based on SSC, there are four situations related to the update of Γ . First, one zero element of \mathbf{x} changes to nonzero value, indicating the

related liver shape in the repository should be used to represent the input shape. Second, one nonzero element of \mathbf{x} shrinks to zero, which means the related liver shape in the repository should not be used to represent the input shape. Third, one zero element of \mathbf{e} changes to nonzero value. It means that a gross error, which may be caused by mis-segmentation or erroneous detection, is captured by SSC and the gross error should be added to the related vertex. Fourth, one nonzero element of \mathbf{e} shrinks to zero, indicating the corresponding gross error in the former iteration should be removed, and the new iteration verifies that no gross error is related to that element of \mathbf{e} .

Assuming there are s elements in Γ , calculating a new direction that $\mathbf{x}'_{(\lambda)}$ moves towards amounts to solving a linear system of equations of size $s \times s$. In one iteration, if there are n_1 shapes in the repository used to represent the input shape, and the number of non-zero elements in error \mathbf{e} is n_2 , then the matrix that needs to be inverted only contains $n_1 + n_2$ elements, and $n_1 + n_2 = s$. When s is small, the computational complexity is not dominated by matrix inversion operations, but by other matrix multiplications which has a complexity near to $O((n+m) \times s)$. However, the matrix inversion contributes to most of the cost of interior point methods, which has a complexity of $O((n+m)^3)$. In SSC, the solution is sparse, s will be much less than $(n+m)$, which makes the computational efficiency of homotopy will be dramatically higher than that of interior point methods. Thus, the homotopy method can significantly boost the computational efficiency compared with traditional SSC.

2.5. Updating the modeling on the fly

Supposing there are n' new training shapes added to the current repository D , thus we get an expanded repository $\tilde{D} = [D D']$. We denote the representation coefficient vector for the new repository as $\tilde{\mathbf{x}} \in R^{n+n'}$. It can be stacked with \mathbf{e} to form a new vector $\mathbf{x}'' \in R^{n+n'+m}$. We define $\tilde{A} = [\tilde{D} I(m)] \in R^{m(n+n'+m)}$. Thus, Eq. (3) is updated as:

$$\arg \min_{\mathbf{x}''} F_{(\lambda)}(\mathbf{x}'') = \arg \min_{\mathbf{x}''} \left\{ \frac{1}{2} \|\mathbf{y}' - \tilde{A}\mathbf{x}''\|_2^2 + \lambda \|\mathbf{x}''\|_1 \right\} \quad (8)$$

where $\|\mathbf{x}''\|_1 = \|\tilde{\mathbf{x}}\|_1 + \xi \|\mathbf{e}\|_1$.

Instead of re-computing the new optimal solution by decreasing λ from ∞ to 0 again, we employ a more efficient homotopy strategy, which takes advantage of the optimal solution of Eq. (3) that has been achieved before the arrival of new training shapes. Supposing the optimization of Eq. 3 converged with a certain value of λ and the corresponding optimal solution was \mathbf{x}' . We set λ in Eq. (8) to a small fixed value, and define a new vector:

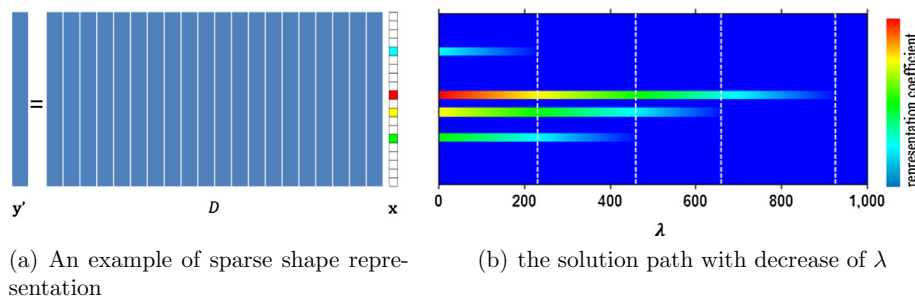


Fig. 2. An illustration of the property of homotopy. In (a), an input shape is constructed by a sparse composition of shapes in the repository. The gross error is zero and the optimization problem is simplified to just deal with \mathbf{x} . The homotopy algorithm starts with a large value of λ . In (b), shows the change of the solution with decrease of λ . White dot lines are where break points appear. The amplitude of representation coefficients is shown in different colors. (For interpretation of the references to colour in this figure legend, the reader is referred to the web version of this article.)

$$\bar{\mathbf{x}}'' \in \mathbb{R}^{n+n'+m} : \bar{\mathbf{x}}''_j = \begin{cases} \bar{\mathbf{x}}'_j & 1 \leq j \leq n \\ 0 & n < j \leq n+n' \\ \bar{\mathbf{x}}'_{j-n-n'} & n+n' < j \leq n+n'+m \end{cases} \quad (9)$$

We consider the following problem:

$$\arg \min_{\mathbf{x}''} F_{(\omega)}(\mathbf{x}'') = \arg \min_{\mathbf{x}''} \left\{ \frac{1}{2} \|\mathbf{y}' - \tilde{A}\mathbf{x}''\|_2^2 + \lambda \|\mathbf{x}''\|_1 + (1-\omega) \mathbf{u}^T \mathbf{x}'' \right\} \quad (10)$$

where $\mathbf{u} = -\lambda \mathbf{z} - \tilde{A}^T(\tilde{A}\bar{\mathbf{x}}'' - \mathbf{y}')$ and \mathbf{z} is a vector that is defined as $\text{sgn}(\bar{\mathbf{x}}'')$ on the support set of $\bar{\mathbf{x}}''$. ω is a factor in the range of 0 to 1. The subdifferential of $F_{(\omega)}(\mathbf{x}'')$ is:

$$\partial F_{(\omega)}(\mathbf{x}'') = \tilde{A}^T(\tilde{A}\bar{\mathbf{x}}'' - \mathbf{y}') + \lambda \partial \|\mathbf{x}''\|_1 + (1-\omega) \mathbf{u} \quad (11)$$

When $\omega = 0$, the optimal solution for Eq. (10) is obviously $\bar{\mathbf{x}}''$. Supposing the optimal solution for Eq. (8) is $\bar{\mathbf{x}}''$. when ω changes from 0 to 1, the problem of Eq. (10) will gradually deform to the one of Eq. (8), and the optimal solution for Eq. (10) will gradually deform from the warm-start vector $\bar{\mathbf{x}}''$ to the desired solution $\bar{\mathbf{x}}''$. Similar to the situation in Eq. (3), the solution path of \mathbf{x}'' also follows a continuous, piece-wise-linear function of ω . For a given value of ω , the optimal solution of \mathbf{x}'' is completely determined by its support set and the sign sequence. The support set of \mathbf{x}'' will change only at some break-points of ω .

Compared with solving Eq. (8) directly by identifying a decreasing sequence of λ , indirectly solving Eq. (10) by identifying an increasing sequence of ω will be more efficient in the case of shape modeling on the fly, where n' , the number of new coming training shapes, is often far smaller than n , the capacity of previous repository. At each iteration, homotopy method needs to update one element of its support set. The support set of $\bar{\mathbf{x}}''$ and that of $\bar{\mathbf{x}}''$ usually have many common elements, thus it needs far fewer iteration for the optimal solution to deform from $\bar{\mathbf{x}}''$ to $\bar{\mathbf{x}}''$ (related to an increasing sequence of ω) than deform from zero to $\bar{\mathbf{x}}''$ (related to a decreasing sequence of λ). Since the shape representation problem is sparse, the time consumed in each iteration is relatively low for both of these two methods. As a result, it will be very fast to achieve the new optimal solution by solving the problem of Eq. (10) when new training shapes arrive.

In summary, our proposed framework aims to model complex liver shapes with high accuracy and efficiency, and achieve efficient shape modeling on the fly. On one hand, SSC can deal with complex variation of liver shapes by overcoming the limitation of parametric possibility distribution. It also explicitly models gross errors in the input shape and captures mis-segmented regions more effectively. One the other hand, we use a homotopy-based method to solve the optimization problem in SSC at a fast speed. It also allows liver shape modeling using large-scale training data and high number of vertices, which will further improve the accuracy. When new training shapes are added to the repository, the homotopy method can update the optimal solution on the fly in a fast speed, avoiding re-computing the solution from scratch.

3. Results

3.1. Experimental setting

In the experiments, we validated our algorithm in liver surgical planning system and measured its accuracy and efficiency when modeling liver shape priors. The adaptive focus deformable model (AFDM) (Shen et al., 2001) was used to obtain one-to-one correspondence of vertices on different meshes. All the experiments were performed on a 2.67 GHz Workstation with 12 cores and 48G RAM, and the algorithms were in MATLAB implementation. We compared the computational cost of LP, FISTA and homotopy

methods when they converged to the same accuracy of $1e-5$, and compared the accuracy of homotopy-based SSC with SSM using Principle Component Analysis (PCA).

3.2. Evolution of SSC's output based on homotopy method

Fig. 3 shows an example of the evolution of SSC's output at different break points in homotopy method. The input liver shape contained an over-segmented part near the heart, which could be treated as gross error. As shown in the figure, at a high value of λ , the over-segmented part was almost excluded, but the error of modeling was large. With the decrease of λ , several break points appeared. At each break point, with the change of Γ , either one element of the representation coefficient of training shapes or one element of gross errors is updated. This led to the update of SSC's output and the improvement of accuracy.

3.3. Computational efficiency based on synthetic input shape

Assuming there are s non-zero elements in the optimized solution of \mathbf{x}' in Eq. (3), we define non-sparsity index of the liver repository with respect to the input liver shape as s . In order to investigate the performance of homotopy method when the non-sparsity index varied, we employed synthesized input shapes in the experiment at first. For a given value of $s = n1 + n2$, a synthesized vector \mathbf{y}' could be constructed by a linear combination of $n1$ randomly selected columns of matrix A , followed by adding a gross error which had $n2$ non-zero elements. This synthesized vector was converted to a shape, which was taken as the input shape.

Fig. 4(a) shows the number of iterations needed by Homotpy and FISTA when the non-sparsity index varied in a large range. The capacity of repository was 500 and vertex number was set as 800. The non-sparsity index ranged from 10 to 500. At each parameter set, we measured the average number of iterations of FISTA and homotopy for 20 synthesized input vectors. It was shown that for homotopy method, the number of iterations was nearly a piece-wise linear function of non-sparsity index. In Fig. 4(a), when the non-sparsity index was low, for example, less than 250, the number of iterations was equal to non-sparsity index. This means when the shape representation problem is sparse to a certain degree, the number of iterations is equal to the sum between the number of shapes in the repository that are used to represent the input shape and the whole number of gross errors on the input shape. When the non-sparsity index was higher, for example, larger than 300, the number of iterations was increasingly larger than the non-sparsity index, and the difference between them also rose with the increase of non-sparsity index. In contrast, for FISTA, it was shown by Fig. 4(a) that the number of iterations was not affected by the non-sparsity index when the repository's capacity and number of vertices were fixed.

The corresponding runtime of these two methods are shown in Fig. 4(b). The runtime of FISTA just slightly fluctuated around 4.0 s, but homotopy had a large range of runtime, from nearly 0.1s to 10.7 s. When the non-sparsity index was larger than 350, homotopy obviously spent more time to solve SSC than FISTA, and with the increase of non-sparsity index, the runtime of homotopy also increased fast. However, when the problem was sparser (the non-sparsity index was less than 350), homotopy had a great advantage of computational efficiency over FISTA. The more sparsely an input shape could be represented by a given repository, the less runtime was needed by homotopy to solve SSC. Thus, homotopy is more suitable to solve sparse problems related to shape representation.

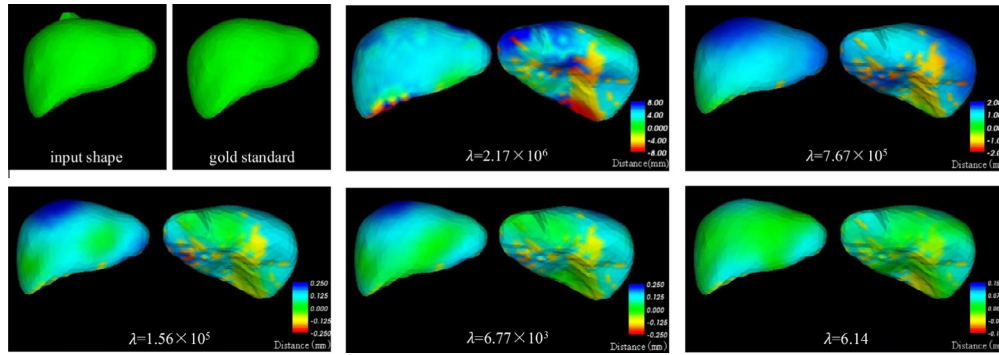


Fig. 3. Evolution of SSC's output based on homotopy method. The input shape contained an over-segmented part. Each picture shows the output of SSC at one break point of homotopy. The outputs were compared with gold standard, and the distance errors were shown in different colors (repository capacity was 60, and vertex number was 800). (For interpretation of the references to colour in this figure legend, the reader is referred to the web version of this article.)

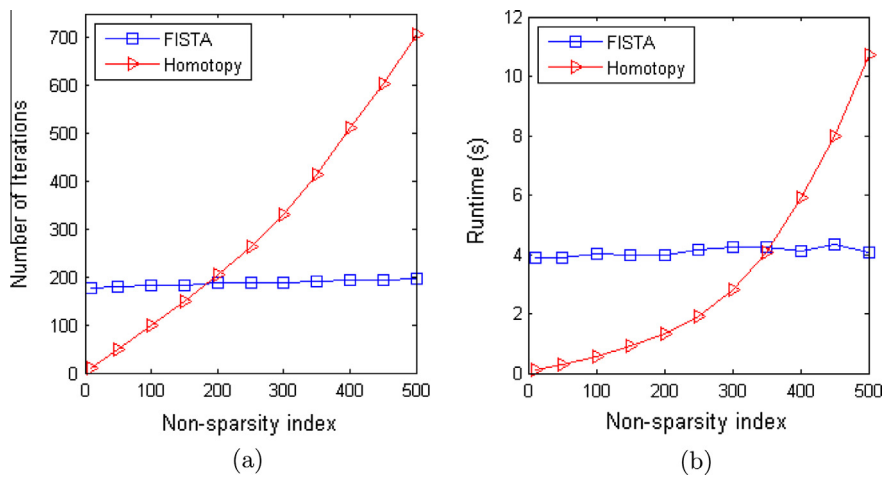


Fig. 4. The change of iteration number (a) and runtime (b) with the increase of non-sparsity index. (repository capacity was 500, and vertex number was 800).

3.4. Computational efficiency based on clinical input shape

In the following experiments, input liver shapes were obtained from clinical CT data. We collected image data of 20 individuals. 7 of them were normal persons, and others had intrahepatic tumors. The tumors were distributed in different parts of livers, such as in the left lobe, in the middle bottom part of liver, or close to major hepatic vessels. The tumors usually had lower gray levels than normal hepatic tissues, and some of them made the liver shape deform to a large degree. The slice thickness of CT data was 1.25 mm. Image resolution was 512×512 , and pixel spacing was $0.8574 \text{ mm} \times 0.8574 \text{ mm}$. To model liver shapes, a rough liver segmentation based on simple region growing method was rapidly performed firstly. The segmentation results were then converted to meshes and registered to the reference shape in the repository.

To evaluate the efficiency and scalability of our method, we need a large repository of training liver shapes, with many vertices on each shape, which is necessary for modeling complex liver shapes and details. In other words, the matrix D in Eq. (1) should have both large number of rows and columns. Specifically, we set the range of repository's capacity to 1000 to 10,000 (i.e., number of shapes), and the maximum vertex number to 2000, which should be sufficiently large for evaluating the scalability of our method. However, collecting such number of livers and manually segmenting them to get training shapes may not be feasible at current stage. In practice, training samples in the repository were synthesized from clinical data of 100 individuals, whose livers were

manually segmented and converted to meshes. These shapes could be taken as the corresponding gold standards of these livers. We employed PCA to compute the parameter vector of these shapes' distribution and then randomly sampled the parameter space to generate a large number of training samples. Since SSC did not rely on the distributional model of training shapes, when we focused on the computational cost of different optimization algorithms, using synthesized training samples would not have an effect on the measurement of time consumptions.

The average runtimes for LP, FISTA and homotopy are shown in Fig. 5. The results were based on the average performance on 20 cases for each algorithm. Firstly, we tested the performance of these algorithms when the number of vertices was fixed and the repository's capacity changed. In Fig. 5(a), the number of vertices was set as 800. It was shown that with the increase of the repository's capacity, the time consumed by FISTA and LP rose rapidly. In contrast, the homotopy method had a relatively slow increase of runtime with the rise of repository's capacity. When the repository's capacity increased from 1000 to 10,000, homotopy method had a runtime ranging from 1.43 s to 3.53 s, but the time consumed by FISTA increased from 5.49 s to 30.65 s, and LP consumed 25.67 min to 96.60 min, which showed the great advantage of homotopy when dealing with large-scale shape repository.

Fig. 5(b) shows the change of runtime for LP, FISTA and homotopy with the increase of vertex number. The capacity of repository was fixed as 500. When the number of vertices was low, all of these three algorithms had a low computational cost. It should be

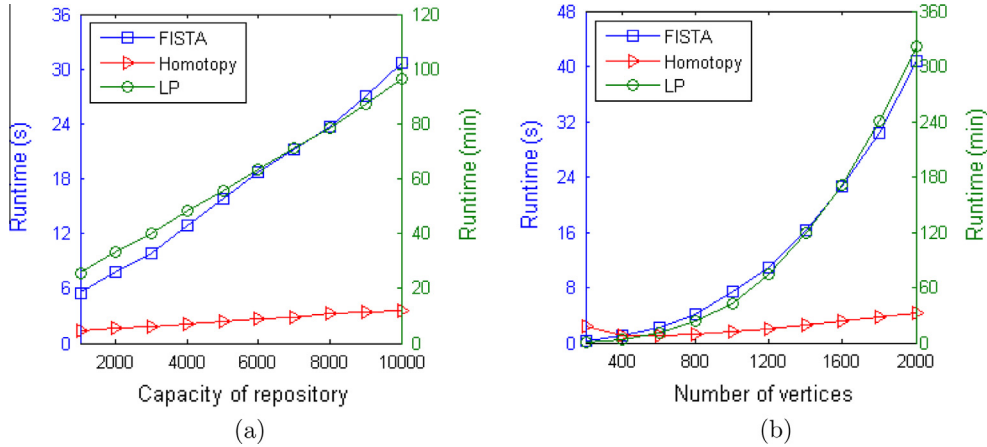


Fig. 5. The change of runtime with the increase of repository's capacity and vertex number. In (a), the vertex number was fixed to 800, and repository's capacity increased from 1000 to 10,000. In (b), repository's capacity was fixed to 500, vertex number increased from 200 to 2000. Note that the runtime of LP is in minute, as shown in the green axis on right. (For interpretation of the references to colour in this figure legend, the reader is referred to the web version of this article.)

noticed that when the number of vertices was set as 200, the runtime of homotopy was higher than that of FISTA, and it decreased when the number of vertices increases to 400. This could be explained by the property of homotopy shown by Fig. 4(b) as discussed above: at a low value of vertex number, the length of \mathbf{x}' in Eq. (3) was also low, and the ratio between number of non-zero elements in \mathbf{x}' and the length of \mathbf{x}' was relatively high, thus the solution was actually not so sparse. As a result, homotopy method would need more iterations to converge to the solution.

It was shown in Fig. 5(b) that when the vertex number became greater, the computational cost of all these algorithms increased. However, FISTA and LP had an obvious sharp rise of runtime with the increase of vertex number, while the runtime of homotopy method increased very slowly. When the number of vertices increased from 200 to 2000, homotopy method had a runtime ranging from 0.96 s to 4.38 s, but the time consumed by FISTA increased from 0.34 s to 40.69 s, and LP consumed 0.38 min to 322.21 min. From Figs. 5(a) and (b), it can be shown that homotopy method remains very high computational efficiency when repository's capacity and vertex number increase to a large scale. We further measured the runtime of the three algorithms in the case where the repository's capacity was enlarged to 10,000 and the vertex number was set as 2000, and the result showed that homotopy just cost about 11.29 s, while FISTA and LP cost 176.82 s and 387.36 min respectively. This means that in such a large-scale condition, homotopy is about 2000 times faster than interior point method.

3.5. The sensitivity of parameters and homotopy's advantage in parameter setting

The optimization problem in Eq. (1) has a constraint that the error term $\|\mathbf{y}' - \mathbf{D}\mathbf{x} - \mathbf{e}\|_2$ should be less than a given number η . We define $\eta^* = \eta / \|\mathbf{y}'\|_2$. The relative error between input shape and SSC represented shape is $\varepsilon = \|\mathbf{y}' - \mathbf{D}\mathbf{x} - \mathbf{e}\|_2 / \|\mathbf{y}'\|_2$. Thus the constraint in Eq. (1) is equal to the condition $\varepsilon \leq \eta^*$. For a certain value of error parameter η^* , there exists a value of $\lambda(\eta^*)$ that makes Eqs. (1) and (2) have the same solution. When SSC is employed for liver shape modeling, one usually sets η^* to a given value, and the corresponding value of $\lambda(\eta^*)$ in Eq. (2) should also be found. For many methods to solve Eq. (2), that value may be obtained by testing a large range of possible values of λ in its parameter space and choosing the one that makes the constraint in Eq. (1) is satisfied. However, this process is time consuming.

Compared with other methods to solve the L_1 -norm optimization problem in SSC, homotopy has an advantage that it naturally searches the desired value of λ during its iterations. At the start of homotopy method, the value of λ is large, which means the optimization problem favors the sparsity of \mathbf{x} and \mathbf{e} , and the corresponding relative error $\varepsilon(\lambda)$ is also large. With the increase of iteration numbers, homotopy will regulate λ to a lower value when the algorithm finds a new break point, which favors the relative error $\varepsilon(\lambda)$ between the input shape and SSC represented shape, and $\varepsilon(\lambda)$ will also become lower. Thus homotopy can be used to identify the λ that corresponds to the given value of η^* . To obtain the desired $\lambda(\eta^*)$, the algorithm computes the relative error $\varepsilon(\lambda)$ after getting each break point of λ . If $\varepsilon(\lambda)$ is larger than the target error of η^* , the algorithm continues to compute the next break point. If $\varepsilon(\lambda)$ is less than η^* after k th iteration, the algorithm uses linear interpolation to find the desired $\lambda(\eta^*)$ which makes the relative error equal to η^* .

$$\lambda(\eta^*) = \lambda^{(k-1)} + \frac{\eta^* - \varepsilon^{(k-1)}}{\varepsilon^{(k)} - \varepsilon^{(k-1)}} (\lambda^{(k)} - \lambda^{(k-1)}) \quad (12)$$

Fig. 6 shows an example of the function of ε versus $\log(\lambda)$. The vertex number was set as 800, and repository capacity was 100. Fig. 6 plotted the value of $\log(\lambda)$ and the corresponding value of relative error ε at the end of each iteration. Break points were denoted as stars in that figure. In Fig. 6(a), the rightmost star denotes the first iteration, and the leftmost star denotes the last iteration. Fig. 6(b) is one part of Fig. 6(a) that was zoomed in. As an example, we set η^* to $1e-3$. Point P_k denotes the value of λ and ε at the end of k th iteration, where the relative error is less than $1e-3$. Point P_{k-1} denotes the value of λ and ε at the end of $(k-1)$ th iteration, where the relative error is larger than $1e-3$. As a byproduct of homotopy, the target value of $\lambda(\eta^*)$ can be determined by point P_k and P_{k-1} using Eq. (12), as shown in Fig. 6(b). In addition, it should be noticed that when λ varied in the range of 0.001 to 1000, the relative error kept a low value that was less than $1e-5$ as shown in Fig. 6(a). This means that the optimal solution have a high accuracy when λ decreased to less than 1000, and it not sensitive to parameter value of λ in a large range, which makes it general for different input shapes in the same application of liver shape modeling.

3.6. Computational efficiency of shape modeling on the fly

To update shape modeling on the fly, we gradually added new training shapes to the repository. We compared efficiency of two

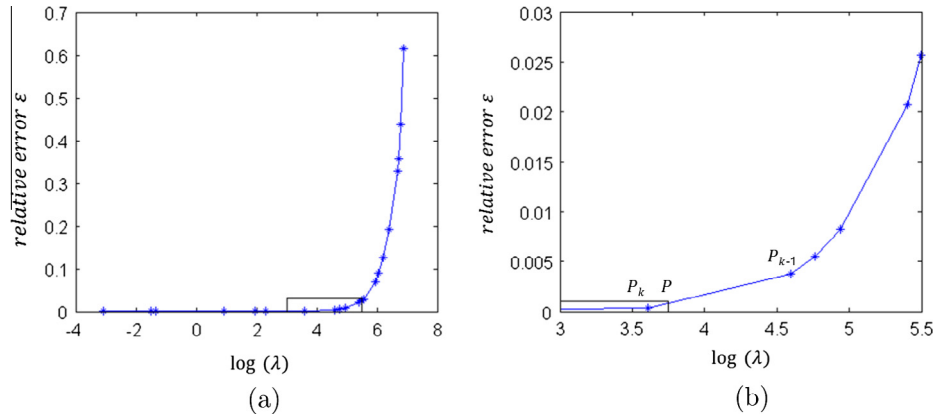


Fig. 6. An example of the function of ε versus $\log(\lambda)$. (b) is one part of (a), which is denoted as a rectangle in (a). Notice that the value of $\log(\lambda)$ and ε after the first iteration are denoted as the rightmost star in (a).

methods for obtaining the new optimal solution after the repository's expansion. The first method solved the optimal solution for Eq. (10) with ω deforming from 0 to 1, and it employed the optimal solution obtained before the arrival of new training shapes. The second method just re-computed the solution for Eq. (8), with a starting vector of zero. The vertex number was set as 800. The initial capacity of repository was 9000, and it was gradually expanded to 10,000, by 100 each time. We employed liver shapes of 20 individuals as testing data. In the repository's i th expansion, the capacity changed from $9000 + (i - 1) * 100$ to $9000 + i * 100$, we used $dt(i)$ to denote the time consumed by updating the optimal solution. The accumulated time $t(i) = t(0) + \sum_{\tau=1}^i dt(\tau)$ denotes the accumulation of runtime for all the i expansions, including the time consumed by computing the optimal solution for the initial shape repository, which is denoted as $t(0)$.

The average updating time $dt(i)$ and accumulated time $t(i)$ for all the testing data are shown in Fig. 7. At the start, there were 9000 shapes in the repository, and the runtime of homotopy-based SSC was $t(0) = 3.3732$ s. In the first expansion, 100 new training shapes were added to the repository. For the first method mentioned above, $dt(1) = 0.7920$ s, while for the second method, $dt(1) = 3.6677$ s. This is shown by the leftmost points on the two curves in Fig. 7(a). With the continuous increase of repository's capacity, $dt(i)$ for the first method kept less than 0.8 s. In contrast, $dt(i)$ for the second method maintained higher than 3.6 s, which showed that updating based on Eq. (10) was far more efficient than re-computing the optimal solution for Eq. (8) in cases where new training shapes arrived. The accumulated time $t(i)$ is shown in

Fig. 7(b), which more obviously showed the difference between these two methods. After 10 expansions, the repository's capacity was expanded to 10,000, and the average accumulated time $t(10)$ for the first method was 10.8891 s, while for the second method, $t(10) = 41.8113$ s.

3.7. Evaluation of the accuracy for liver shape prior modeling

Fig. 8 shows the result of liver shape prior modeling using homotopy-based SSC, which was compared with PCA shape prior. The middle and rightmost column in Fig. 8 show a visualization of errors of the modeling, and the errors were measured as the shortest Euclidean surface distance from modeling result to gold standards, which were acquired from manual segmentation results. The red color shows under-segmented regions and blue color shows over-segmented parts. The repository's capacity was set as 800 and the vertex number was set as 1500. In the first row, the postcava led to an over-segmentation, and both SSC and PCA excluded that region. It should be noticed that PCA shape prior lost some local details at the corner of left liver lobe. However, SSC shape prior successfully preserved these parts, which can be seen from the visualized distance errors: the PCA shape prior had more red regions than SSC shape prior. The input shape in the second row had an over-segmentation in the heart region and an under-segmentation in the liver's inner side. These regions were gross errors in the input liver shape. However, the output of PCA did not effectively exclude the heart region and restore the inner side accurately. In contrast, these gross errors were successfully

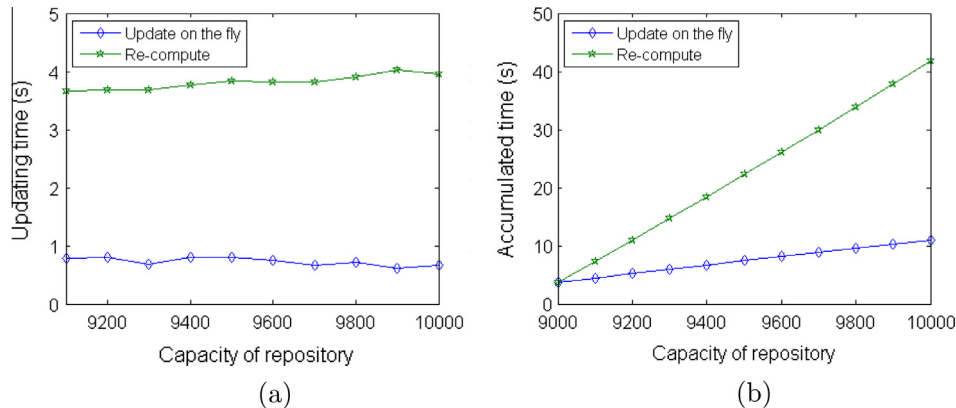


Fig. 7. The averaged updating time (a) and accumulated time (b) with the repository's capacity gradually expanding from 9000 to 10,000. Note that (b) is the integration of (a).

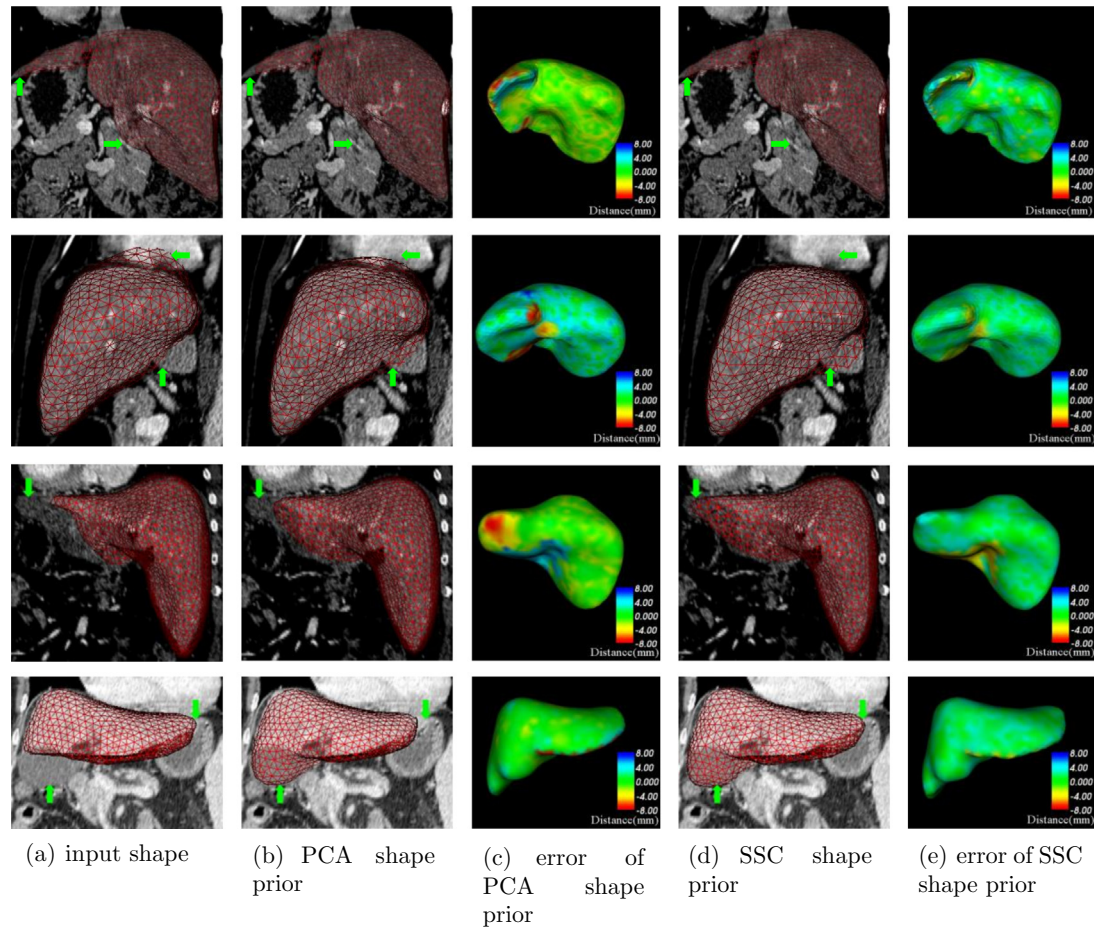


Fig. 8. Visualization of SSC shape prior and PCA shape prior. First and second row: shape modeling results of healthy cases. Third and fourth row: shape modeling results of livers with tumors.

captured and excluded by SSC. The result showed that SSC overcome the influence of the heart more effectively than PCA, and SSC also had a better performance in restoring the under-segmented parts in the input shape. The last two cases in Fig. 8 showed shape prior modeling results for patients with liver tumors. In the third row, the patient had a tumor in the left liver lobe, which was under-segmented in the initial shape mainly due to its different gray scale than normal liver tissues. PCA shape prior restored most parts of the tumor region, but it failed to reserve the corner of the liver. However, SSC shape prior almost exactly modeled the real shape of the liver. In the last row of Fig. 8, a tumor appeared in the middle lower side of the liver, PCA shape prior performed well in preserving the tumor region, but it lost some local details. In contrast, SSC achieved more accurate results, with local details being preserved well.

To evaluate the accuracy of our shape prior modeling method quantitatively, we measured the dice similarity coefficient (DSC), the average symmetric surface distance (ASD) and maximum symmetric surface distance (MSD).

$$DSC = \frac{2 \times TP}{2 \times TP + FN + FP} \quad (13)$$

where TP, FN, FP denote true positive, false negative and false positive respectively. For two liver shapes, we use S_0 and S_1 to represent the set of surface points on each shape respectively. s_0 is an arbitrary point in S_0 , and s_1 is an arbitrary point in S_1 . $d(s_0, S_1)$ is the shortest Euclidean distance between the point s_0 and the surface S_1 .

$$ASD = \frac{1}{|S_0| + |S_1|} \left(\sum_{s_0 \in S_0} d(s_0, S_1) + \sum_{s_1 \in S_1} d(s_1, S_0) \right) \quad (14)$$

$$MSD = \max \left\{ \max_{s_0 \in S_0} d(s_0, S_1), \max_{s_1 \in S_1} d(s_1, S_0) \right\} \quad (15)$$

We measured the mean value and standard deviation of DSC, ASD and MSD for the 20 individuals, and reported the accuracy of shape priors based on PCA and SSC. Both PCA and SSC shape priors were compared with gold standards. The results are shown in Table 1. PCA shape priors had a good DSC and ASD result, but it had a high MSD value (the average MSD was more than 10 mm), which indicated that some local parts of the liver was not well preserved by PCA. In contrast, the SSC shape priors had an obviously higher DSC, and far lower ASD and MSD (the average MSD was less than 4 mm). It is shown that SSC can model liver shape priors quite accurately.

Table 1

Quantitative evaluation of liver shape prior modeling based on PCA and SSC. We reported the mean values and standard deviations of dice similarity coefficient (DSC), average symmetric surface distance (ASD), and maximum symmetric surface distance (MSD).

| | DSC (%) | ASD (mm) | MSD (mm) |
|-----|--------------|-------------|--------------|
| PCA | 88.27 ± 7.52 | 2.28 ± 1.34 | 10.36 ± 4.82 |
| SSC | 94.31 ± 3.04 | 1.12 ± 0.69 | 3.65 ± 1.40 |

4. Discussion

The experiments show the following advantages of homotopy-based SSC for shape prior modeling in liver surgical planning system.

1. The homotopy-based SSC can achieve patient-adaptive liver shape priors effectively. First, liver shapes have very complex variations, but SSC is able to handle them by overcoming the limitation of parametric possibility distribution used in many traditional methods. Second, the challenges in liver segmentation make the input shape easily contain over-segmented regions adjacent to other organs such as the heart, or under-segmented regions. Since our proposed method explicitly models gross errors, it can capture them and be robust to mis-segmented regions. In addition, it has the ability to preserve local details, especially some corners and inner parts of liver shapes, which makes the shape prior be more patient-adaptive.
2. Compared with traditional SSC, the proposed homotopy-based SSC achieves high efficiency by taking advantage of two sparsity observations in liver shape modeling. First, the representation coefficient vector \mathbf{x} for shapes in the repository is sparse, which means the input liver shape can be approximately represented by a linear combination of only a very small subset of the repository. Second, the gross error \mathbf{e} that we explicitly model is sparse, which means the gross errors related to mis-segmentations may be large but also relatively sparse compared with the whole liver shape. Since the computational efficiency of homotopy is proportional to the sparsity of a problem, these properties make homotopy more suitable to deal with liver shape representation.
3. Homotopy-based SSC is promising for highly accurate and efficient liver shape modeling. Homotopy method speeds up the optimization process in SSC dramatically compared with traditional algorithms, and the high computational efficiency makes it possible to model accurate liver shape priors in real-time clinical environment. In addition, livers' surfaces have many corners and uneven parts, representing details of which needs a relatively high number of vertices, and some liver patterns are rare, which makes the repository should contain as many kinds of liver shapes as possible. Using a higher number of vertices and larger scale of training data will help better modeling local details of clinical liver. The related large-scale computation can be compensated by low runtime of homotopy, which increases very slowly when the scale of training shapes and number of vertices rise to a large degree.
4. Homotopy naturally searches the appropriate parameter set during its iterations, and further improves the computational efficiency compared to other methods which find the appropriate parameter set by an extra independent process. In addition, the proposed model is not sensitive to parameter set of λ . It allows users to set its value in a large range without obvious effect on accuracy of the optimal solution.
5. To update the shape modeling on the fly, we change the strategy of homotopy and take advantage of the optimal solution obtained before the arrival of new training shapes. It avoids re-computing the optimal solution from scratch, and just needs few iterations to deform to the new solution when the problem is sparse, which is suitable for SSC shape modeling. This method significantly decreases the solution's updating time when new training shapes arrive

gradually. Thus, it can be used for modeling of liver shapes on the fly, which is more applicable in clinical environment since training shapes are usually not obtained in one batch.

5. Conclusion

In this paper, we introduced a efficient homotopy-based SSC to model liver shape priors in liver surgical planning system. It addresses three important problems in patient-specific liver shape modeling: (1) obtain accurate shape priors, (2) be scalable and remain high efficiency when dealing with large-scale training data, and (3) achieve the updated optimal solution on the fly when new training shapes arrive gradually. This method represents an input shape by an optimized sparse combination of shapes in the repository and continuously transforms the optimization problem into a series of simplified problems whose solution is fast to compute. Experiments showed that the proposed method had a high performance in dealing with complex liver shape variations, excluding gross errors and preserving local details on the input shape. Its runtime increased very slowly with the rise of the scale of training data and number of vertices. In conditions where the repository's capacity was very large and the number of vertices was very high, the new method showed a great advantage of quickly achieving accurate liver shape priors. With more training shapes being added gradually, homotopy can update the optimal solution of SSC on the fly, without re-computing the optimal solution from scratch. When the computational efficiency is boosted, SSC becomes more promising to be smoothly applied in clinical environments, with its fast speed, high accuracy and scalability. It should be noticed that the new optimization method for SSC is general and it can benefit other applications as well.

Acknowledgements

This research is partially supported by the Chinese NSFC research fund (61190120, 61190124 and 61271318) and biomedical engineering fund of Shanghai Jiao Tong University (YG2012ZD06).

References

- Afonso, M.V., Bioucas-Dias, J.M., Figueiredo, M.A., 2011. An augmented lagrangian approach to the constrained optimization formulation of imaging inverse problems. *IEEE Trans. Image Process.* 20, 681–695.
- Asif, M.S., Romberg, J., 2013. Sparse recovery of streaming signals using l1-homotopy. *CoRR abs/1306.3331*.
- Beck, A., Teboulle, M., 2009. A fast iterative shrinkage-thresholding algorithm for linear inverse problems. *SIAM J. Imag. Sci.* 2, 183–202.
- Broelsch, C.E., Malago, M., Testa, G., Gamazo, C.V., 2000. Living donor liver transplantation in adults: outcome in europe. *Liver Transplant.* 6, s64–s65.
- Chambolle, A., Pock, T., 2011. A first-order primal-dual algorithm for convex problems with applications to imaging. *J. Math. Imag. Vis.* 40, 120–145.
- Chartrand, R., Wotao, Y., 2008. Iteratively reweighted algorithms for compressive sensing. In: *IEEE International Conference on Acoustics, Speech and Signal Processing, 2008 (ICASSP 2008)*. IEEE, pp. 3869–3872.
- Chen, J.G., Zhang, S.W., 2011. Liver cancer epidemic in china: past, present and future. In: *Seminars in Cancer Biology*. Elsevier, pp. 59–69.
- Cootes, T.F., Taylor, C.J., 1999. A mixture model for representing shape variation. *Image Vis. Comput.* 17, 567–573.
- Cootes, T.F., Taylor, C.J., Cooper, D.H., Graham, J., 1995. Active shape models-their training and application. *Comput. Vis. Image Underst.* 61, 38–59.
- Cremers, D., Rousson, M., Deriche, R., 2007. A review of statistical approaches to level set segmentation: integrating color, texture, motion and shape. *Int. J. Comput. Vis.* 72, 195–215.
- Daubechies, I., Defrise, M., De Mol, C., 2004. An iterative thresholding algorithm for linear inverse problems with a sparsity constraint. *Commun. Pure Appl. Math.* 57, 1413–1457.
- Davatzikos, C., Tao, X., Shen, D., 2003. Hierarchical active shape models, using the wavelet transform. *IEEE Trans. Med. Imag.* 22, 414–423.
- Donoho, D.L., Tsai, Y., 2008. Fast solution of l1-norm minimization problems when the solution may be sparse. *IEEE Trans. Inform. Theory* 54, 4789–4812.

- Etyngier, P., Segonne, F., Keriven, R., 2007. Shape priors using manifold learning techniques. In: IEEE 11th International Conference on Computer Vision, 2007 (ICCV 2007). IEEE, pp. 1–8.
- Foucart, S., Rauhut, H., 2013. *A Mathematical Introduction to Compressive Sensing*. Springer, New York, NY, USA.
- Gao, Y., Liao, S., Shen, D., 2012. Prostate segmentation by sparse representation based classification. *Med. Phys.* 39, 6372–6387.
- Ghose, S., Oliver, A., Mart, R., Llad, X., Freixenet, J., Mitra, J., Vilanova, J., Comet-Batlle, J., Meriaudeau, F., 2012. Statistical shape and texture model of quadrature phase information for prostate segmentation. *Int. J. Comput. Assist. Radiol. Surg.* 7, 43–55.
- Hamarnah, G., Li, X., 2009. Watershed segmentation using prior shape and appearance knowledge. *Image Vis. Comput.* 27, 56–98.
- Heimann, T., van Ginneken, B., Styner, M.A., Arzhaeva, Y., Aurich, V., Bauer, C., Beck, A., Becker, C., Beichel, R., Bekes, G., 2009. Comparison and evaluation of methods for liver segmentation from ct datasets. *IEEE Trans. Med. Imag.* 28, 1251–1265.
- Heimann, T., Meinzer, H.P., 2009. Statistical shape models for 3d medical image segmentation: a review. *Med. Image Anal.* 13, 543–563.
- Heimann, T., Wolf, I., Meinzer, H.P., 2006. Active shape models for a fully automated 3d segmentation of the liver. An evaluation on clinical data. In: *Medical Image Computing and Computer-Assisted Intervention*. (MICCAI 2006). Springer, pp. 41–48.
- Leventon, M.E., Grimson, W.E.L., Faugeras, O., 2000. Statistical shape influence in geodesic active contours. In: *Proceedings of IEEE Conference on Computer Vision and Pattern Recognition*, 2000. IEEE, pp. 316–323.
- Malioutov, D.M., Cetin, M., Willsky, A.S., 2005. Homotopy continuation for sparse signal representation. *Proceedings of IEEE International Conference on Acoustics, Speech, and Signal Processing*, 2005 (ICASSP'05), vol. 5. IEEE, pp. v/733–v/736.
- Nesterov, Y., 1983. A method of solving a convex programming problem with convergence rate $o(1/k^2)$. In: *Soviet Mathematics Doklady*, pp. 372–376.
- Osborne, M.R., Presnell, B., Turlach, B.A., 2000. A new approach to variable selection in least squares problems. *IMA J. Numer. Anal.* 20, 389–403.
- Rousson, M., Paragios, N., 2000. Shape priors for level set representations. In: *Computer Vision. ECCV-2002*. Springer, pp. 78–92.
- Shen, D., Herskovits, E.H., Davatzikos, C., 2001. An adaptive-focus statistical shape model for segmentation and shape modeling of 3-d brain structures. *IEEE Trans. Med. Imag.* 20, 257–270.
- Shi, F., Wang, L., Wu, G., Li, G., Gilmore, J.H., Lin, W., Shen, D., 2014. Neonatal atlas construction using sparse representation. *Human brain mapping*.
- Shi, Y., Qi, F., Xue, Z., Chen, L., Ito, K., Matsuo, H., Shen, D., 2008. Segmenting lung fields in serial chest radiographs using both population-based and patient-specific shape statistics. *IEEE Trans. Med. Imag.* 27, 481–494.
- Sotiropoulos, G.C., Drhe, N., Sgourakis, G., Molmenti, E.P., Beckebaum, S., Baba, H.A., Antoch, G., Hilgard, P., Radtke, A., Saner, F.H., 2009. Liver transplantation, liver resection, and transarterial chemoembolization for hepatocellular carcinoma in cirrhosis: which is the best oncological approach? *Digest. Diseases Sci.* 54, 2264–2273.
- Trzasko, J., Manduca, A., 2009. Highly undersampled magnetic resonance image reconstruction via homotopic-minimization. *IEEE Trans. Med. Imag.* 28, 106–121.
- Vu, N., Manjunath, B.S., 2008. Shape prior segmentation of multiple objects with graph cuts. In: *IEEE Conference on Computer Vision and Pattern Recognition*, 2008 (CVPR 2008). IEEE, pp. 1–8.
- Wang, G., Zhang, S., Gu, L., 2014. Scalable sparse shape composition and its application to liver surgical planning. In: *2014 IEEE 11th International Symposium on Biomedical Imaging (ISBI)*, pp. 377–380.
- Wang, G., Zhang, S., Li, F., Gu, L., 2013. A new segmentation framework based on sparse shape composition in liver surgery planning system. *Med. Phys.* 40, 051913.
- Wright, J., Ma, Y., Mairal, J., Sapiro, G., Huang, T.S., Yan, S., 2010. Sparse representation for computer vision and pattern recognition. *Proc. IEEE* 98, 1031–1044.
- Xie, J., Jiang, Y., Tsui, H.t., 2005. Segmentation of kidney from ultrasound images based on texture and shape priors. *IEEE Trans. Med. Imag.* 24, 45–57.
- Yan, P., Xu, S., Turkbey, B., Kruecker, J., 2010. Discrete deformable model guided by partial active shape model for trus image segmentation. *IEEE Trans. Biomed. Eng.* 57, 1158–1166.
- Yan, P., Xu, S., Turkbey, B., Kruecker, J., 2011. Adaptively learning local shape statistics for prostate segmentation in ultrasound. *IEEE Trans. Biomed. Eng.* 58, 633–641.
- Yang, A.Y., Sastry, S.S., Ganesh, A., Ma, Y., 2010. Fast l1-minimization algorithms and an application in robust face recognition: a review. In: *17th IEEE International Conference on Image Processing (ICIP)*, 2010. IEEE, pp. 1849–1852.
- Yu, Y., Zhang, S., Huang, J., Metaxas, D., Axel, L., 2013. Sparse deformable models with application to cardiac motion analysis. In: *Gee, J., Joshi, S., Pohl, K., Wells, W., Zlei, L. (Eds.), Information Processing in Medical Imaging, Lecture Notes in Computer Science*, vol. 79. Springer, Berlin Heidelberg, pp. 208–219.
- Zhang, S., Zhan, Y., Dewan, M., Huang, J., Metaxas, D.N., Zhou, X.S., 2012a. Towards robust and effective shape modeling: sparse shape composition. *Med. Image Anal.* 16, 265–277.
- Zhang, S., Zhan, Y., Metaxas, D.N., 2012b. Deformable segmentation via sparse representation and dictionary learning. *Med. Image Anal.* 16, 1385–1396.
- Zhang, W., Yan, P., Li, X., 2011. Estimating patient-specific shape prior for medical image segmentation. In: *International Symposium on Biomedical Imaging*. IEEE, pp. 1451–1454.
- Zhu, Y., Papademetris, X., Sinusas, A.J., Duncan, J.S., 2009. A dynamical shape prior for lv segmentation from rt3d echocardiography. In: *Medical Image Computing and Computer-assisted Intervention*. (MICCAI 2009), pp. 206–213.